A Simulation Method for Thermal Infrared Imagery from Moon-Based Earth Observations

Jingjuan Liao, Linan Yuan, and Chenwei Nie

***Abstract*—As a unique natural satellite of the Earth, the Moon has always attracted much attention, and one subject of interest is the establishment of an Earth observation platform on the Moon. Compared with the existing spaceborne and airborne observation platforms, a Moon-based Earth observation platform would have the unique advantage of the ability to obtain global and large-scale observation data. At present, the study on Moon-based Earth observations is in theory, so it is necessary to use simulation methods to understand the observation performance of a Moon-based Earth observation platform. In this study, a method for Moon-based Earth observation imaging simulation in the thermal infrared band is developed to study the Moon-based thermal infrared imaging process. The method comprises three parts, including the estimation of Moon-based imaging coverage, the acquisition of the radiation intensity at the entrance pupil, and the simulated image output from the Moon-based thermal infrared sensor. Then, the simulated results are validated with the existing spaceborne observation data. Results show that the absolute error of Moon-based thermal infrared simulations is between 1.3-5.7 K, the RMSE is between 1.38 - 3.12 K, and the relative error is between 0.44% - 2.12%, indicating that the thermal infrared imaging model can more realistically simulate the true conditions of ground surface and that a Moon-based Earth observation platform could observe the Earth in the thermal infrared band.**

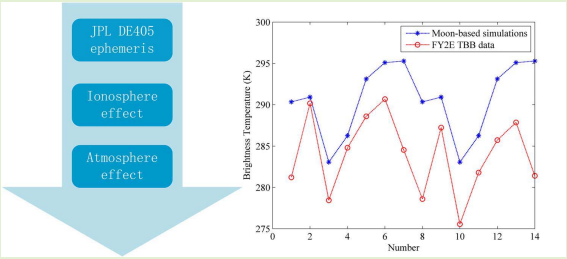

***Index Terms*— Moon-based Earth observation, thermal infrared imaging simulation, radiance, land surface temperature, thermal infrared.**

I. Introduction

REMOTE sensing technology is currently a unique tool for quickly achieving global or large-scale Earth observations due to its global, fast, quantitative, and periodic characteristics, so it has been used in many fields such as resources, environment, socioeconomics, and national security. However, spaceborne Earth observation platforms, such as polar orbit satellites, geostationary satellites, and the Deep Space Climate Observatory (DSCOVR), have many limitations regarding acquiring global-scale data. Polar orbit satellites have high spatial resolution but low temporal resolution due to their limited orbit height and coverage, so they cannot quickly acquire global-scale Earth observation data. The coverage can be expanded by image mosaicking, but the spatial and temporal consistency of mosaic result cannot be satisfied due to various acquisition times. Geostationary satellites have high temporal resolution but cannot observe polar region, even if there are multiple geostationary satellites. The DSCOVR located at the Sun-Earth L1 point has low spatial resolution and cannot achieve global-scale Earth observations at night. Moreover, the service lives of polar orbit satellites, geostationary satellites, and DSCOVR are limited by the manufacturing technology, space environment, and low orbital height, causing difficulty in achieving long-term and stable observations for Earth.

The Moon, a natural satellite of the Earth, has gradually attracted attention owning to its unique orbital features. Recently, much attention has been paid to the establishment of a Moon-based Earth observation platform. Palle and Goode analyzed the lunar-based Earth observation platforms and artificial satellite platforms from the aspects of the field of view, spatial resolution, observation angle, revisit period and service life. They found that Moon-based Earth observations had obvious superiorities in monitoring climate change, such as the ability to make global observations, various observation angles, and long operating life [1]. Ding *et al.* analyzed in detail the coverage and spatial resolution of Moon-based imaging radar through a simplified observation model and

Manuscript received November 26, 2020; accepted December 25, 2020. Date of publication January 11, 2021; date of current version February 17, 2021. This work was supported in part by the National Natural Science Foundation of China under Grant 41590855 and in part by the Key Research Project in Frontier Science of the Chinese Academy of Sciences under Grant QYZDY-SSW-DQC026. The associate editor coordinating the review of this article and approving it for publication was Prof. Shih-Chia Huang. *(Corresponding author: Linan Yuan.)*

Jingjuan Liao is with the Aerospace Information Research Institute, Chinese Academy of Sciences, Beijing 100094, China (e-mail: liaojj@radi.ac.cn).

Linan Yuan and Chenwei Nie are with the Aerospace Information Research Institute, Chinese Academy of Sciences, Beijing 100094, China, and also with the College of Resources and Environment, University of Chinese Academy of Sciences, Beijing 100049, China (e-mail: yuanln@radi.ac.cn; niecw@radi.ac.cn).

Digital Object Identifier 10.1109/JSEN.2021.3049912

simulated the Moon-based radar detection range of the Amazon Plain as well as the Qinghai-Tibet Plateau. Results showed that a Moon-based imaging radar system could completely cover the Qinghai-Tibet Plateau most of the time, and the time coverage of the Amazon Plain was 40% -70%, indicating good coverage performance [2]. Zhang established a Sun-Earth-Moon simulation system and found that a Moon-based Earth observation platform could monitor real-time global changes by acquiring global observation data in a short time [3]. Ding *et al.* simulated and analyzed differences in speed, space coverage, viewable range and time coverage from different remote sensing platforms, such as solar synchronous orbit, tilted geosynchronous orbit, and lunar orbit, based on similar satellite orbit simulation methods. The results showed that Moon-based Earth observation platforms had good space-time coverage characteristics and observation angles in the middle and low latitudes [4]. Using the Jet Propulsion Laboratory (JPL) high-precision ephemeris DE405 and a spatial coordinate transformation, they developed a Doppler parameter estimation method for the Moon-based Synthetic Aperture Radar (SAR) system. The results showed that the beam angle needed continuous adjustment along the orbit to point to the Earth disk in the Moon-borne SAR case, and the antenna position displacement leaded to a significant shift in the Doppler parameters [5]. Ye *et al*. [6] analyzed the coverage of the Moon-based Earth observations using the JPL ephemeris data. The results showed that Moon-based Earth observation had large effective coverage, wide swath, and continuous observation ability which can conduce to global change monitoring. Ren *et al*. [7] presented the reference system transformation and a simulation system of Moon-based Earth observations based on the Jet Propulsion Laboratory ephemerides. Through numerous experiments and a series of simulation images, it was proved that the lunar observatory had continuous observation characteristics and wide swath. Guo *et al*. [8] presented a geometric image model and evaluated the influence of the exterior orientation elements on the geolocation errors of an optical sensor. Yuan and Liao [9] analyzed in detail four influence factors on Moon-based microwave radiation imaging, including the time zone correction, relative movement of the Earth-Moon, atmospheric radiative transfer effect, and ionosphere effect. Then they simulated Moon-based microwave brightness temperature images and evaluated the results using the multichannel Advanced Microwave Scanning Radiometer (AMSR-E) data. Li *et al*. [10] proposed two processing methods of optical sensors imaging from the Moon-based Earth observation platform for global change based on the optical sensors' capability and Moon-based orbital characteristics. To conduct the geometric correction of images from Moon-based platform, Zhang *et al.* developed a polar coordinate system on a Moon-based nadir, and solved the geometric distortion problems from the Earth's curvature, nadir changes, and the wavy terrain [11]. Overall, the Moon-based Earth observation platform has unique superiority in obtaining global and large-scale surface parameters, including various solar zenith angles, azimuth angles, as well as sensor viewing angles, and the Moon-based platform can instantaneously observe about half of the Earth's surface. In addition, Moon-based Earth observation platforms have high temporal resolution and long service lives, indicating that a Moon-based platform is suitable for observation of macro-scientific phenomena, including land surface temperature, solid Earth tides [12], and Earth's radiation balance [13]. Theoretically, a complete observation of the Earth can be carried out in short time along with the Earth-Moon relative movement. Therefore, the new Earth observation method can effectively compensate for the shortcomings in acquiring Earth observation data by existing satellites.

At present, the theoretical research on Moon-based Earth observations is just at the beginning stage without actual observation data, and the study on Moon-based Earth observations of the thermal infrared band has not yet been carried out. To understand the thermal infrared observation capability of a Moon-based Earth observation platform, the entire imaging process needs to be studied by a simulation method. In previous studies, many simulation methods have been developed for remote sensing imaging, and the existing methods are mainly applicable to polar orbit satellites. Schott *et al.* proposed a digital imaging and remote sensing image generation model (DIRSIG), and simulated visible or thermal infrared multispectral and hyperspectral images by image synthesis technology [14]. Using the Multispectral Infrared and Visible Imaging Spectrometer (MIVIS) data, Ye *et al.* simulated the images from SPOT-HRV, XS1, XS2, and XS3 through spectral simulation and atmospheric correction, then evaluated them with the true measurements. Results showed that the SPOT-HRV simulations had a higher accuracy than other bands. To analyze the spectral sensitivity and atmospheric effects on various sensors, he also simulated the apparent reflectance images and ground-reflectance images at corresponding bands of three sensors, e.g., SPOT-HRV, CBERS-CCD, NOAA14-AVHRR, and Landsat-TM [15], [16]. Börner *et al.* developed a Software Environment for the Simulation of Optical Remote sensing systems (SENSOR) which described the sensor hardware itself, the observed scene, and the atmosphere effect, and verified the simulation results in the Airborne PRISM Experiment (APEX) project supported by the European Space Agency [17]. Yang *et al.* developed a high-resolution mid-infrared imaging simulation system for spaceborne satellites using the atmospheric radiation model MODTRAN4, and a preliminary examination proved that the simulation model had better accuracy [18]. Stephen *et al.* described the Aerospace Corporation's Parameterized Image Chain Analysis & Simulation Software (PICASSO) a simulation model for the infrared band that can evaluate the imaging quality through the parameters of the sensor [19], [20]. Pandya *et al.* used the atmospheric radiative transfer model MODTRAN to simulate at-sensor radiance for thermal channels of Imager payload onboard INSAT-3D satellite [21]. Using atmospheric radiation transmission models and imaging models, Zhao proposed a simulation model for aerospace infrared remote sensing imaging system by constructing a surface thermal infrared radiation scene [22]. Segl *et al.* developed simulation software that could analyze data acquisition, sensor calibration, and data processing of Sentinel-2 satellites [23]. Verhoef and Bach simulated the images from Sentinel-3 sensors using a land

scene generator (LSG) model [24]. Gastellu developed a three-dimensional radiation transmission simulation model (DART). By constructing three-dimensional ground scenes, it can simulate the images under different atmospheric conditions and sensor responses [25]–[27]. From these studies, we find that each remote sensing imaging models are developed for an imaging system integrated with a certain type of spaceborne platform and the viewing zenith and atmospheric effect are basically small or constant in each image [28]–[34]. However, Moon-based Earth observations have various viewing zenith angles and atmospheric effects in every image, and the effect of the ionosphere cannot be ignored due to the high orbital attitude of Moon-based platform. Therefore, the current remote sensing imaging models cannot directly apply to Moon-based Earth observation platforms.

To understand the thermal infrared observation properties for a Moon-based Earth observation platform, a thermal infrared imaging simulation method for Moon-based Earth observation was developed in view of the characteristics of the observation platform, and the thermal infrared image from the Moon-based Earth observation platform were simulated. In this study, the simulation includes three parts, e.g., the estimation of Moon-based imaging coverage, the acquisition of the radiation intensity at the entrance pupil of the Moon-based sensor, and the simulated image output from the Moon-based thermal infrared sensor. Then the Moon-based simulation results are validated with the existing thermal infrared remote sensing data obtained from a satellite. Further, this paper compared the simulation method with other methods. This study would provide supporting for the construction of Moon-based thermal infrared sensors and their applications in the future.

II. Data Used in This Study

A. Global Land Surface Temperature (LST) Observed From the Moon-Based Platform

The global LST observed from the Moon-based platform was obtained by time correction. Based on the diurnal variation characteristics of the LST under sunny conditions, the NIE17 model was used for the time correction to estimate the global LST acquired at the same coordinated universal time [35]. The global LST observed by the Moon-based Earth observation platform is mainly concentrated in the regions of 60°S to 60°N, except for extreme weather conditions and areas. In addition, the global LST images can cover about half of the Earth's surface, and the imaging position varies from east to west with the relative movement of Earth and Moon. The observation time (coordinated universal time, UTC) of every pixel is the same. In this study, the global LST is used for simulating the thermal infrared image of the Moon-based Earth observation platform.

B. Global Land Elevation Data

Global surface elevation data with spatial resolution similar to that of LST data were selected to estimate the surface radiation scene and atmospheric radiation in this study. The elevation data are global land one-kilometer base elevation (GLOBE) data released by the National Centers for Environmental Information (NCEI) of the National Oceanic and Atmospheric Administration (NOAA), with equal latitude and longitude projections and a spatial resolution of 30°, and can be acquired from the website: https://www.ngdc.noaa.gov/mgg/topo/globeget.html.

C. Brightness Temperature Data From FY-2 Satellite

The Fengyun-2 (FY-2) weather satellite is the first generation of geostationary orbit weather satellite developed by China, and it includes eight satellites, e.g., FY-2A, FY-2B, FY-2C, FY-2D, FY-2E, FY-2F, FY-2G, and FY-2H, which were launched in June 1997, June 2000, October 2004, December 2006, December 2008, January 2012, December 2014, and June 2018, respectively. The equivalent blackbody brightness temperature (TBB) data from a Visible and Infrared Spin Scan Radiometer (VISSR) consistent with the simulated time (January 1 to 3, 2015) were selected to verify the results of thermal infrared imaging simulation for the Moon-based Earth observation platform. The VISSRs aboard FY-2E and FY-2F satellites have five bands, including bands 1 (far-infrared, 10.29 - 11.45 μm), band 2 (far-infrared, 11.59 - 12.79 μm), band 3 (mid-infrared, 6.32 - 7.55 μm), band 4 (mid-infrared, 3.59 - 4.09 μm), and band 5 (near-infrared, 0.510 - 0.905 μm), and has a time resolution of 30 minutes and a spatial resolution of 5 km at the nadir. The TBB data with full disk nominal (NOM) format can be obtained from the National Satellite Meteorological Center (NSMC) of the China Meteorological Administration (http://satellite.nsmc.org.cn/portalsite/Data/Satellite.aspx).

III. Methods

The thermal infrared imaging simulation of Moon-based Earth observation platform comprises three parts, including the estimation of Moon-based imaging coverage, the acquisition of radiation intensity at the entrance pupil of Moon-based sensor, and the simulated image output from Moon-based thermal infrared sensor. In the paper, the Moon-based Earth observation platform is assumed to be set in the nadir of the Moon, and the JPL DE405 ephemeris data are selected to estimate the position of Moon-based nadir at different times. Then, the solar elevation angle and viewing zenith angle of the Moon-based thermal infrared sensor can be estimated through these parameters such as the Earth's curvature, longitude, latitude, date, elevation, and time. The spatial coverage of the Moon-based Earth observation are the areas where the solar elevation angle is bigger than zero. In addition, the thermal infrared image from the Moon-based Earth observation platform is resampled to the same spatial resolution as that of the MOD11C3 product.

A. The Radiance at the Entrance Pupil of the Moon-Based Thermal Sensor

As a key part of the Earth-space environment, the ionosphere exists in the areas of 90 km to 1000 km above the Earth's surface, and is composed of many ions and free electrons. Due to the limited orbital heights of many satellite platforms, the spaceborne thermal infrared imaging generally need not consider the ionosphere effect. However, a Moon-based platform is located outside Earth's ionosphere, which

can cause the changes in the propagation path of thermal infrared radiation and radiation energy attenuation due to the collisions between neutral particles, ions, and electrons. Therefore, the influence of ionosphere on thermal infrared radiation needs to be analyzed in this study. Since the ionosphere is in the geomagnetic field, the ionosphere mentioned here refers to plasma with an applied magnetic field. The dielectric tensor of a uniform magnetized plasma is as (1), shown at the bottom of the page, where $\bar{\varepsilon}_r$ is the dielectric tensor of a uniform magnetized plasma, ω_p is plasma frequency, ω is the electromagnetic wave angular frequency, ω_{ce} is the electron cyclotron frequency, j is the imaginary unit, υ_e is the collision frequency between electrons and neutral gas molecules, θ is the viewing zenith angle, and e is the magnitude of electron charge. The attenuation coefficient of electromagnetic waves in plasma is:

$$\alpha = -\frac{\omega}{c} I\mathrm{m}\left(\sqrt{\bar{\varepsilon}_r}\right) \tag{2}$$

where α is the attenuation coefficient of electromagnetic waves in plasma, ω is the electromagnetic wave angular frequency, c is the velocity of light, and Im is the imaginary part of propagation constant. The power attenuation can be expressed as:

$$Att = 8.69\alpha z(dB) \tag{3}$$

where α is the attenuation coefficient of electromagnetic waves in plasma, z represents the thickness of the ionosphere. The frequency change caused by the ionosphere can be calculated by the formula:

$$\Delta f = \frac{-b}{2\pi\omega c} \cdot \frac{d\int_0^z Ndl}{dt} \tag{4}$$

where b is 1.6×10^3 mks, ω is the electromagnetic wave angular frequency, c is the velocity of light, N is the electron concentration, z represents the thickness of the ionosphere, and t is the plasma temperature.

Moreover, in the estimation of the radiance at the entrance pupil of the Moon-based thermal sensor, the atmospheric effect is the main factor and needs to be analyzed. Since the scattering and absorption caused by the water vapor and aerosols in the atmosphere, the thermal radiation generated by the Earth's surface can be weakened when it reaches the sensor's entrance pupil. The atmosphere is also an infrared radiation source that generates upwelling and downwelling radiation. The atmospheric downward radiation first reaches the ground surface and is reflected by the ground surface. Then, through atmospheric absorption attenuation, the atmospheric downward radiation together with the atmospheric upward radiation at the top layer of the atmosphere is received by the Moon-based thermal infrared sensors, causing an increase in the radiation energy at the sensor's entrance pupil. The spectral radiance received by the high-altitude observation platform (the radiance at the entrance pupil, units: $w \cdot sr^{-1} \cdot cm^{-2}$) at the viewing angle (θ, φ) can be expressed as [20], [23], [36]–[39]:

$$I_i(\theta,\varphi) = I_R(\theta,\varphi)\,\tau_i(\theta,\varphi) + R_{at_i\uparrow}(\theta,\varphi) \tag{5}$$

and $I_R(\theta,\varphi)$ is the spectral radiation received by Earth's surface with units of $w \cdot sr^{-1} \cdot cm^{-2}$, which can be expressed as:

$$I_R(\theta,\varphi) = \varepsilon_i(\theta,\varphi)\, I_B(T_s) + (1-\varepsilon_i(\theta,\varphi))\,\frac{R_{at_i\downarrow}}{\pi} \tag{6}$$

where ε_i is the spectral emissivity of Earth's surface, τ_i is atmospheric transmittance, T_s is LST, $I_B(T_s)$ is the thermal infrared radiation from Earth's surface with units of $w \cdot sr^{-1} \cdot cm^{-2}$, i is frequency, $R_{at_i\uparrow}$ is atmospheric upward radiation, and $R_{at_i\downarrow}$ is atmospheric downward radiation.

The Moon-based Earth observation platform is at the theoretical stage, and the relevant thermal infrared sensor has not been developed. In this study, MODIS 31 and 32 (TIR Band 1, TIR Band 2) are selected as the operating bands of the thermal infrared sensor of the Moon-based Earth observation platform, and their spectral ranges and spectral response functions are shown in Figure 1. Then the atmospheric radiation transmission model MODTRAN is used to simulate the radiance image at the entrance pupil of the thermal infrared sensor of the platform. The input parameters of the MODTRAN model include atmospheric profile data, atmospheric parameters, carbon dioxide content, aerosol type, water vapor content, land surface emissivity, land elevation, and viewing zenith angle. The atmospheric profile data uses the default data in the MODTRAN model. Since the atmospheric parameters of each pixel depend on the latitude and time, the subarctic winter atmospheric parameters, mid-latitude winter atmospheric parameters, tropical atmospheric parameters, and mid-latitude summer atmospheric parameters from the MODTRAN model are used in the northern hemisphere polar region, northern hemisphere mid-latitude regions, tropical regions, and southern hemisphere mid-latitude regions, respectively. The water vapor and carbon dioxide contents are determined by the actual features of Moon-based Earth observation platform. The aerosol type is set as rural aerosol with a visible distance of 23 km because 23 km is the best weather condition [40], [41]. The values of the MODIS land surface emissivity products have little variation for TIR Band1 or TIR Band2 in different time periods (91% of the land surface emissivity changes within 0.002, and 99.4% of the land surface emissivity changes less than 0.006); thus, the average emissivity from different time periods (including 01:30 am, 10:30 am, 13:30 pm, and 22:30 pm) is used in the MODTRAN model, and the land

$$\bar{\varepsilon}_r = 1 - \frac{\omega_p^2/\omega^2}{\left[1 - j\frac{\upsilon_e}{\omega} - \frac{\frac{\omega_{ce}^2}{\omega^2}sin^2\theta}{2\left(1-\frac{\omega_p^2}{\omega^2}-j\frac{\upsilon_e}{\omega}\right)}\right] \pm \left[\frac{\frac{\omega_{ce}^4}{\omega^2}sin^4\theta}{4\left(1-\frac{\omega_p^2}{\omega^2}-j\frac{\upsilon_e}{\omega}\right)} + \frac{\omega_{ce}^2}{\omega^2}cos^2\theta\right]^{1/2}} \tag{1}$$

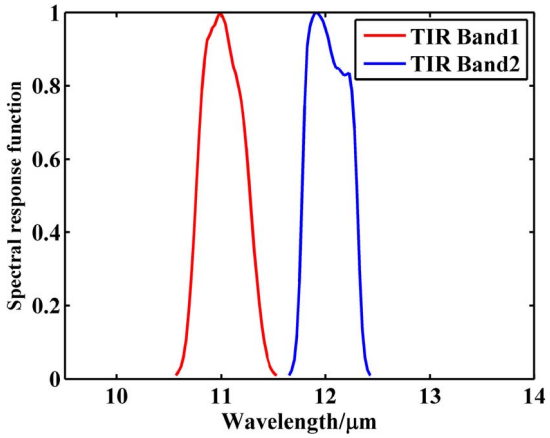

Fig. 1. Spectral response functions of the Moon-based thermal sensor bands.

elevation data (GLOBE data) from the National Environmental Information Center are used for the simulation.

B. The Simulation Image From the Moon-Based Thermal Sensor

Through the effect of the optical sensor system, the irradiance of the focal plane of the thermal infrared sensor for the Moon-based platform can be estimated by the radiation energy of the entrance pupil. Then, a digital signal image processed by remote sensing data processing systems can be output through the photoelectric conversion of the infrared detector (the radiant energy is converted into weak voltage signals) and signal processing, such as amplification, filtering, sampling, and quantization [42]–[44]. During the process of thermal infrared imaging, the radiant energy and imaging quality at the infrared focal plane are related to the transmittance, the effective aperture, and the effective focal length of the optical system, and the output image quality depends on the spectral response of the detector, spatial response, and focal plane nonuniformity. Furthermore, various random noises generated during signal transmission, conversion, and processing [45]–[49] have an impact on the radiation resolution of the image.

The thermal infrared imaging method of the Moon-based Earth observation platform is set as frame imaging. Based on the physical process of the thermal radiation signal inside the sensor, the sensor effect on the thermal infrared imaging of the Moon-based Earth observation platform is analyzed, which mainly includes three parts: the imaging simulation of the optical system, the detector effect simulation, and the signal simulation of the thermal infrared remote sensing image. Because the detector module and signal processing module are related to the manufacturing process, these two parts are not described in this study, and we focus on the sensor optical system and grayscale quantification simulation. The thermal infrared radiation flux reaching the focal plane of the thermal infrared sensor can be expressed as:

$$\mathrm{E} = \frac{\pi \tau}{4F^2} \cdot cos^4\alpha \cdot I_i \tag{7}$$

where E (units :$w \cdot cm^{-2}$) is the thermal infrared radiation flux reaching the focal plane of the thermal infrared sensor; τ is the atmospheric transmittance; F is the F number of the optical sensor system, and $F = f_0/D$, D is the effective aperture of the optical sensor system, in which f_0 is the effective focal length of the optical sensor system and α is the angle between the detection pixel and the central axis in the infrared focal plane; I_i is the radiance at the entrance pupil; and $cos^4\alpha$ is the imaging shadow effect caused by the optical system.

Then through analog to digital conversion (A/D) which contains sampling, holding, quantization and coding, the continuous physical quantity (thermal infrared radiation) can be converted into a binary number that the computer can recognize. The digital number (DN) value of a grayscale image in the thermal infrared band through the photoelectric conversion, operational amplification and quantization of the sensor can be obtained by [18]:

$$DN = NearestInteger\left[\frac{E - E_{min}}{E_{max} - E_{min}} \times \left(2^r - 1\right)\right] \tag{8}$$

where $NearestInteger[\ ]$ is a integer-truncation operation, E is the radiation intensity of a pixel, E_{min} is the minimum radiation intensity of a single pixel within the observation range, E_{max} is the maximum radiation intensity of a single pixel within the observation range, and r is the number of quantization levels after A/D conversion of the infrared imaging system.

In this study, the noise from the imaging process is converted into composite noise and calculated in the signal simulation module. The system noise of the sensor can be expressed as [22]:

$$NETD = \frac{\pi\sqrt{A_d \Delta f}}{A_0 \alpha\beta\tau_0 \int_{\lambda_1}^{\lambda_2} \tau_a(\lambda) D^*(\lambda) \frac{\partial M(T,\lambda)}{\partial T} d\lambda} \tag{9}$$

$$\frac{\partial M(T,\lambda)}{\partial T} = \frac{\left(2\pi hc^2\right)\left(hc/k\right)}{\lambda^6 T^2 \left(e^{hc/\lambda kT} - 1\right)} \tag{10}$$

$$SiTF = G\int_{\lambda_1}^{\lambda_2} \frac{A_0}{4F^2} R(\lambda)\tau(\lambda) \frac{\partial M(T,\lambda)}{\partial T} d\lambda \tag{11}$$

$$\sigma_{sys} = NETD \times SiTF \tag{12}$$

where σ_{sys} is the system noise of sensor, $NETD$ is the equivalent temperature difference of system noise (units: K), $SiTF$ is the system signal transfer function, A_d is the radiation area received by the detector (units: m^2), Δf is the measurement circuit bandwidth (units: MHz), α and β are the plane angles of the instantaneous field of view (horizontal and vertical), τ_0 is the lens transmittance, τ_a is the atmospheric transmittance, $D^*(\lambda)$ is the specific detection rate, T is the target temperature (units: K), G is system gain, F is the F number of optical sensor system, $R(\lambda)$ is the system response rate, λ is the central wavelength of band (units: μm), c represents the speed of light ($2.99793 \times 10^8 m \cdot s^{-1}$), h is the Planck constant ($6.626 \times 10^{-34} J \cdot s$), and k is the Boltzmann constant ($1.3806 \times 10^{-23} J \cdot K$).

IV. Results

A. Estimation of Moon-Based Imaging Coverage

Moon-based Earth observation platform has a special orbit, which affects directly the image coverage at any times

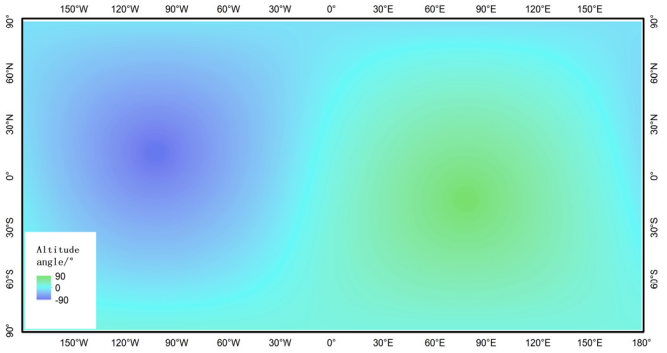

Fig. 2. The viewing altitude angle of the Moon-based Earth observation platform.

from Moon-based Earth observation. The JPL high-precision ephemeris DE405 data records the space position and velocity of the Sun, the Earth (planets), and the Moon in the form of Chebyshev polynomials from 1600 A.D. to 2200 A.D. In this study, given that the Moon-based platform locates in the center of the Moon surface, the ephemeris data was selected to estimate the viewing altitude angle of Moon-based platform, as shown in Figure 2. The areas where the viewing altitude angle is greater than 0° is the viewable areas of the Moon-based Earth observation platform, given in the green in Figure 2. The center of the viewable areas (defined as the nadir) has the altitude angle of 90°, and it gradually decreases to the surroundings, until 0° in the boundary of the visible range.

Generally, the viewing zenith angle is a key parameter and used in most satellite observation. The sum of the viewing zenith angle and the observation altitude angle is 90 degree. Therefore, the viewing zenith angle of the thermal infrared sensor of the Moon-based Earth observation platform is 0-90°, and the nadir has the viewing zenith angle of 0°. For the existing spaceborne thermal infrared sensor, the viewing zenith angle is small, constant, or within 70°. Considering that as the viewing zenith angle increases, the radiance attenuation at the entrance pupil obtained by the thermal infrared sensor of the Moon-based Earth observation platform increases, and the data quality decreases. To obtain effective thermal infrared data from the Moon-based sensors, the spatial coverage of the Moon-based thermal infrared sensor under different viewing zenith angle conditions is analyzed in detail, as shown in Figure 3. Figure 3 (a)-(c) show that the nadir is near 13°S when the viewing zenith angles of the Moon-based Earth observation platforms are less than or equal to 90°, 80°, and 70°, respectively. The Moon-based Earth observation platform can observe all of South America, most of North America, and Antarctica when the zenith angle is less than or equal to 90°. The Earth's surface between 90°S and 75°N could be measured by the Moon-based platform under this condition. The spatial coverage decreases when the viewing zenith angle is less than 80°, but the Moon-based platform can still monitor the Earth's surface from 90°S to 65°N. Moreover, the Moon-based platform can monitor the Earth's surface from 83°S to 55°N with a viewing zenith angle less than 70°.

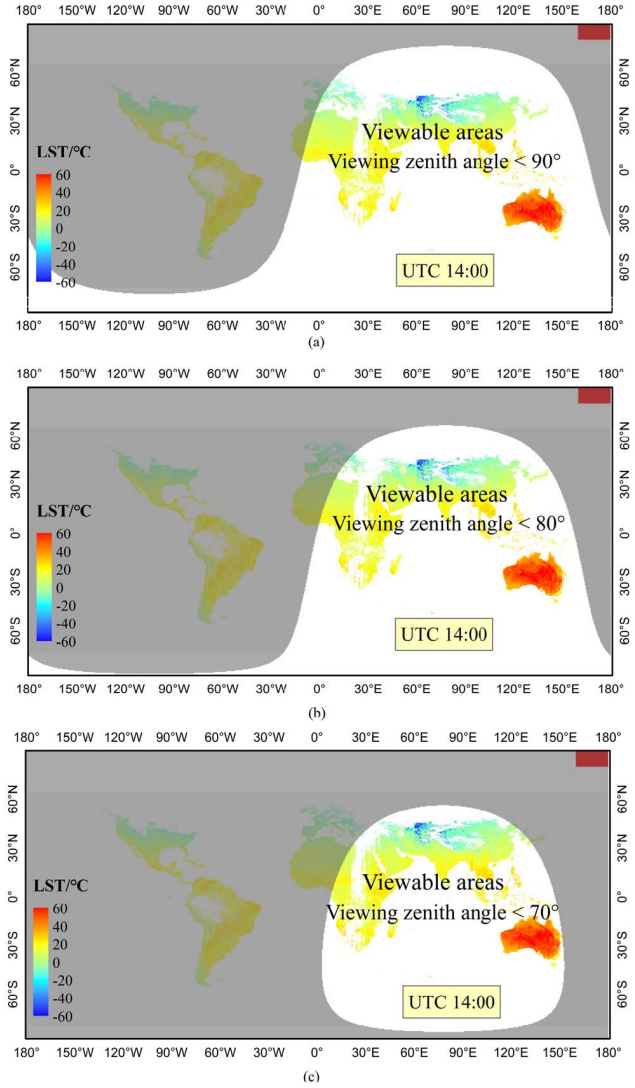

Fig. 3. The spatial coverage of the Moon-based thermal infrared sensor at 14:00 UTC on January 15, 2015 under different viewing zenith angles.

B. The Simulation Results From the Moon-Based Thermal Sensor

In this study, we calculated the effect of the ionosphere from 8 μm-12 μm based on formulas (1)-(4), as figure 4 and 5. Results show that the attenuation and frequency change caused by the ionosphere increases as the wavelength increases. Moreover, the magnitude of the attenuation is 10^{-15} and the frequency change caused by the ionosphere is approximately 10^{-4}, indicating that the value is small. Thus, the ionosphere has little influence on Moon-based thermal infrared imaging simulations, and the atmosphere is the main factor influencing the estimation of the radiance at the entrance pupil of the Moon-based thermal infrared sensor.

Then based on the MODTRAN model and the characteristics of Moon-based Earth observation platform, several factors affecting the radiance at the entrance pupil were analyzed with 8-14 μm wavelengths in this study (Figure 6). Figure 6 shows that the radiation brightness is related to the viewing zenith angle, water vapor content, visible distance, carbon dioxide content, and wavelength. When the atmospheric parameters

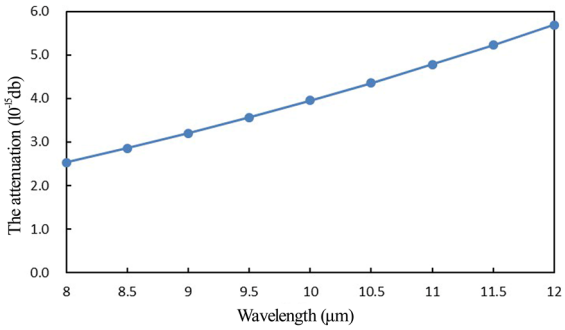

Fig. 4. The attenuation of the thermal infrared bands caused by the ionosphere.

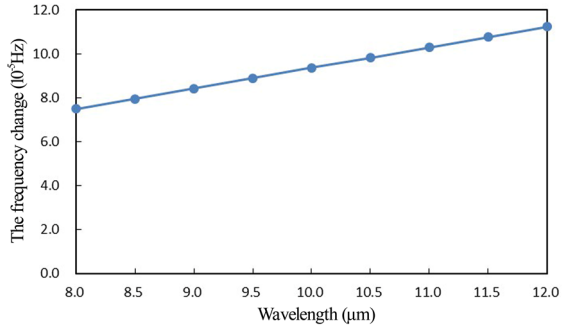

Fig. 5. The ionosphere causes frequency changes in each band of thermal infrared.

are constant, the radiation brightness at the entrance pupil of the Moon-based thermal infrared sensor gradually decreases with increasing viewing zenith angle, and the attenuation rate increases (Figure 6a). The low water vapor content in the atmosphere or the large visible distance leads to an increase in the radiance at the entrance pupil, while the changes in the atmospheric carbon dioxide content have little effect on the radiance at the entrance pupil (Figure 6b-d). Therefore, the viewing zenith angle, water vapor content, and visible distance of the atmosphere must be analyzed in detail, and other atmospheric parameters can be adopted as the default values of the MODTRAN model when calculating the radiance at the entrance pupil.

Based on the global LST in the field of view of the Moon-based Earth observation platform, the radiance at the entrance pupil of the Moon-based Earth observation platform was estimated by the MODTRAN model (Figure 7). The results show that the thermal infrared radiation intensity at the entrance pupil of the Moon-based platform has the same order of magnitude as that of the existing thermal infrared remote sensing data (which is $10^{-4}w \cdot sr^{-1} \cdot cm^{-2}$). The simulated thermal infrared radiation intensity at the entrance pupil has spatial variation characteristics similar to those of the global LST under the field of view of the Moon-based Earth observation platform at the corresponding time. This indicates that the establishment of a thermal infrared Earth observation platform on the Moon can better monitor the spatial distribution of the LST. Further, the radiance at the entrance pupil of Moon-based thermal infrared sensor channel 1 (Figure 7a, MoonTIR1) is slightly greater than that of channel 2 (Figure 7b, MoonTIR2), and MoonTIR1 also

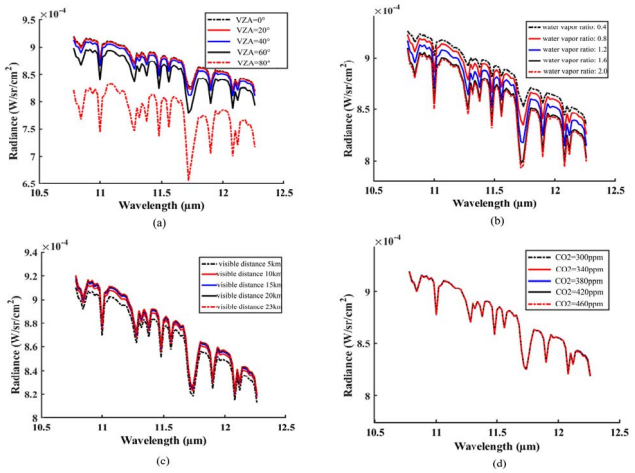

Fig. 6. Analysis of the factors affecting the radiance at the entrance pupil. (a) The viewing zenith angle (VZA); (b) water vapor content; (c) visible distance of the atmosphere; (d) atmospheric carbon dioxide content.

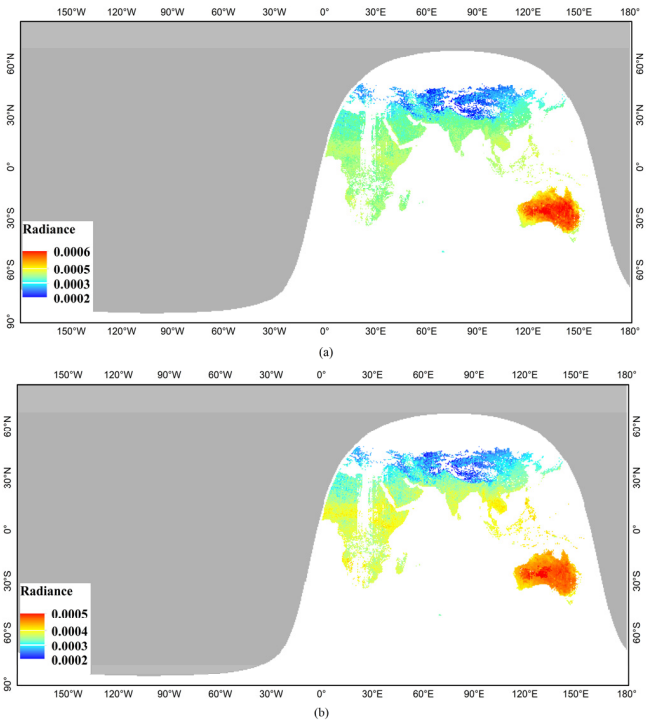

Fig. 7. The simulated radiance at the entrance pupil of the Moon-based Earth observation platform (a. TIR Band 1; b. TIR Band 2).

has a larger variation range of the radiance in the entrance pupil. This is because the center wavelengths of MoonTIR1 and MoonTIR2 are 11 μm and 12 μm, respectively, and the peak surface radiation energy is approximately 10 μm. As the wavelength increases beyond 10 μm, the radiant energy shows a decreasing trend.

In formulas (7) and (8), I_i is the radiance at the entrance pupil of the Moon-based Earth observation platform (Figure 7), E is the irradiance of the focal plane of the thermal infrared sensor, and the DN of formula (8) is the final image of the thermal infrared sensor from the Moon-based Earth observation platform. First, Figure 7 is used to

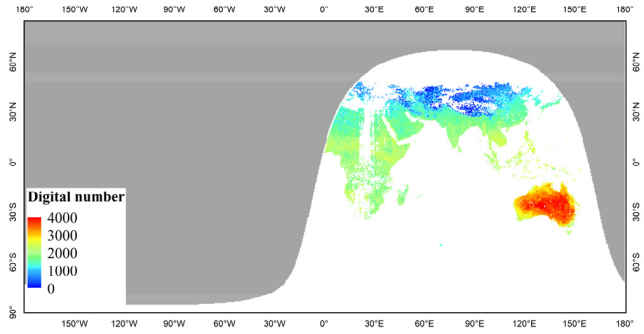

Fig. 8. The simulated image of the Moon-based thermal infrared sensor.

calculate the irradiance of the focal plane of the thermal infrared sensor for the Moon-based Earth observation platform by formula (7). The results show that the irradiance image reaching the focal plane has a spatial distribution trend similar to that of the radiance image at the entrance pupil (Figure 7a) and is significantly smoother. In particular, the areas with low temperature and near the edge of the image have a significantly decreased spatial difference. This is because the radiant energy has a certain attenuation when passing through the lens in the optical system, causing a decrease in the difference between different pixels. Moreover, the energy gathered by the pixels away from the central axis in the focal plane is reduced with increasing distance between the pixels and the center axis in the optical system due to imaging geometry problems. Therefore, the spatial differences in or near the marginal areas are small.

Then, the final simulated image of the thermal infrared sensor from the Moon-based Earth observation platform (Figure 8) was calculated by formula (8) with the A/D sampling number r set as 12. In addition, the focal length, the effective aperture, and the optical transmittance of the thermal infrared sensor of the Moon-based Earth observation platform are set as 2000 mm, 2 m, and 0.5, respectively. Through the analysis of the thermal infrared sensor, the spatial resolution is related to the focal length and the effective aperture. The determination of the focal length shows that the spatial resolution increases with decreasing effective aperture. A small effective aperture requires a large sensor size, but the original panel size is limited due to the material and manufacturing process, causing decreasing spatial resolution. In addition, the spatial resolution increases with decreasing focal length of the thermal infrared sensor. In view of the characteristics and capability of the Moon-based Earth observation platform, the focal length and the effective aperture of the thermal infrared sensor are set as 2000 mm and 2 m, respectively; thus, the spatial resolution is approximately 1 km. Figure 8 shows that the thermal infrared image DN value of the final Moon-based Earth observation platform is highly similar to the radiance image at the entrance pupil, indicating the spatial distribution of the true LST.

C. Validation of Simulation Method Based on FY-2 Data

Since the digital number (DN) value of a grayscale image in the thermal infrared band was obtained through the photoelectric conversion, operational amplification and quantization

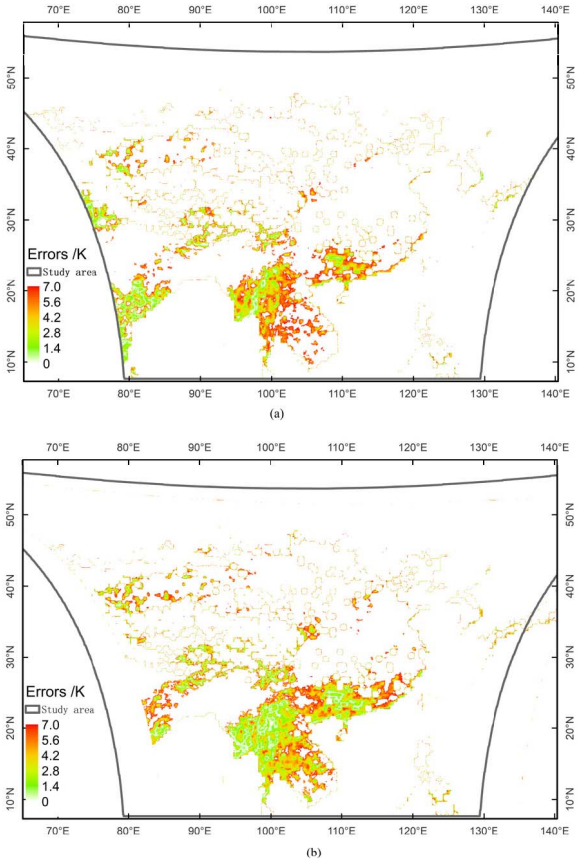

Fig. 9. The errors of the Moon-based thermal infrared simulated brightness temperature with the TBB products from the FY-2 geostationary satellites. (a) Simulation bias based on FY-2E data; (b) simulation bias based on FY-2F data.

of the sensor, there are no suitable thermal infrared data from geostationary satellites for comparison. The equivalent blackbody brightness temperature data from the VISSR consistent with the simulated time (January 1 to 3, 2015) were selected to verify the accuracy of the simulated brightness temperature of the Moon-based thermal sensor, which can be obtained by formulas (5)-(6). Considering the service life of FY-2 geostationary satellites, the VISSR data aboard FY-2E and 2F satellites are suitable for validating the simulation results from the Moon-based thermal infrared sensors. The FY-2 E and F meteorological satellite is positioned at 104.5 and 112 East longitude over the equator, covering one third of the surface and located in the low and middle latitude regions. However, the Moon-based Earth observations can cover about half of the Earth's surface, as shown in Figures 7 and 8. Therefore, to be consistent with the coverage of FY-2, we selected the area in Figure 9 as the study area (70-150°E, 10-55°N) to analyze the accuracy of the Moon-based thermal infrared simulation results. Figure 9 shows the bias of the Moon-based thermal infrared simulated brightness temperature with the TBB products from FY-2 E and F geostationary satellites. The figure shows that the simulation bias is less than 7 K and is significantly low or high in the low latitude region.

Then we analyzed the simulation errors based on 4404 sample points in study area, and the comparison of the Moon-based thermal infrared simulated brightness temperature with

TABLE I
COMPARISON OF THE MOON-BASED THERMAL INFRARED SIMULATION RESULTS WITH FY-2E AND 2F THERMAL INFRARED DATA

Viewing zenith angle/°	FY-2E TBB/K	FY-2F TBB/K	Moon-based simulations/ K	Absolut e error
20	292.86	293.52	291.00	2.19
30	288.23	289.19	290.01	1.30
40	282.07	282.56	286.50	4.19
50	269.92	270.34	274.64	4.49
60	267.69	267.84	272.91	5.14
70	269.76	269.13	275.11	5.70

the TBB products under different viewing zenith angles is shown in Table I. From the table, the absolute error of the Moon-based thermal infrared simulations is 1.3-5.7 K, and the measured brightness temperature is 267.69-293.52 K. Hence, the relative error (which is the ratio of the absolute error to the measured brightness temperature) can be 0.44% - 2.12%. In addition, the simulated value from the Moon-based thermal infrared sensors is slightly larger than the measured TBB from FY-2E geostationary satellite except for the viewing zenith angle of 20°. The uncertainty in the simulation may relate to the selection of atmospheric parameters, especially the water vapor parameters. There are six representative atmospheric modes with significant differences in the MODTRAN model, e.g., sub-Arctic winter, mid-latitude winter, tropical, mid-latitude summer, sub-Arctic summer, and 1976 U.S. Standard mode, each with significantly different water vapor. In addition, the water vapor changes with altitude instead of being constant for each atmospheric mode. Therefore, when we conduct the simulation of the Moon-based Earth observation platform, the whole Earth is divided into four regions based on the latitude and season on January 1, 2015, and every region has a unique water vapor column. However, the water vapor should theoretically be different in different pixels, so this causes some error during the simulation. Moreover, Figure 6 demonstrates that the changes in water vapor column can affect the simulated radiance. In this study, the study area used to evaluate the Moon-based thermal infrared simulation results is located in the low- and middle-latitude regions, so water vapor can cause simulation biases. On the other hand, the Moon-based Earth observation platform has different orbital characteristics from those of the geostationary satellites, so the systematic error of the two observations is different, and the difference between the platforms results in simulation biases.

Furthermore, the accuracy of the thermal infrared imaging results from the Moon-based Earth observation platform were analyzed. Figure 10 shows a comparison of the Moon-based thermal infrared simulations with the TBB data from FY-2E satellites. The viewing zenith angles are 20°, 30°, 40°, 50°, 60°, and 70°, the root mean square errors (RMSEs) of the Moon-based thermal infrared simulations are 1.38 K, 2.71 K, 2.80 K, 3.09 K, 2.96 K, and 2.51 K, respectively. It can be seen that there are no obvious correlations between the error of Moon-based thermal infrared simulations and the viewing zenith angle. In addition, there is a low correlation between the Moon-based TIR simulated data and the TBB observations of FY-2E instruments with viewing zenith angles of 20° and 30°, and the RMSEs are 1.38 K and 2.71 K. As the viewing zenith angle is more than 30°, the Moon-based simulations and FY-2E measurements have a strong correlation.

Figure 11 shows the comparison of the Moon-based simulations with FY-2F TBB data. With the viewing zenith angles of 20°, 30°, 40°, 50°, 60°, and 70°, the RMSEs of the Moon-based thermal infrared simulations are 2.17 K, 2.56 K, 2.94 K, 3.12 K, 2.81 K, and 1.96 K, respectively. There are no obvious correlations between the error of the Moon-based thermal infrared simulations and the zenith angle. Moreover, there is a low correlation between Moon-based TIR simulated data and the TBB observations of the FY-2E instruments with a viewing zenith angle of 20°. As the viewing zenith angle is greater than 20°, the Moon-based simulations and FY-2E measurements have a high correlation.

Figures 10 and 11 show that the viewing zenith angle has a small influence on the accuracy of Moon-based thermal infrared simulation results, and the error between simulation results and FY-2E data is slightly higher than that of FY-2F data. In all, the absolute error of Moon-based thermal infrared simulations is between 1.3 and 5.7 K, and the RMSE is between 1.38 and 3.12 K. Since the simulated brightness temperature is 267.69 - 293.52 K, and the relative error is between 0.44% - 2.12%, the thermal infrared simulation results and method for Moon-based Earth observation platform are reliable [50], and the thermal infrared imaging model of Moon-based Earth observation platform developed in this study can more realistically simulate the real situation of Earth surface, indicating that it is feasible for the Moon-based Earth observation platform to observe Earth in the thermal infrared band.

V. DISCUSSION

In this study, six existing peer's simulation method for thermal infrared imagery, including RS image-simulation method (RSISM) [15], [16], SENSOR approach [17], thermal infrared remote sensing system (TIRSS) [18], PICASSO [19], [20], thermal channels radiance simulation of INSAT-3D sensor (TCRS- INSAT3D) [21], End-To-End Sensor Simulation (ETESS) [23] were selected to compare with the thermal infrared imagery simulation from Moon-based Earth observation. The suitable wavelength, visible distance, aerosol type, solar zenith angle, simulation steps, atmospheric radiative transfer, orbital height of seven simulation were analyzed and detailed results were shown in table II.

It can be seen that seven simulation methods have different suitable wavelength, which are 0.5-1.75, 0.4-2.5, 0.76-1000, 0.45-0.8, 0.55-12.5, 0.44-2.2, and 2.0-1000 μm, respectively. The visible distance of SENSOR is 15 km, and others are 23 km. The rural aerosol type is adopted by six simulation method except TIRSS, and the solar zenith angle are 64.8°, 30°, constant value, 0°, 0-60°, 40°, and 0-90°, respectively. Besides TCRS- INSAT3D, the other existing simulation method have small and constant solar zenith angle. This is because the existing methods are applicable to the satellites which have low orbital height, limited view sight, and small scan width. The TCRS- INSAT3D is used to simulate the satellite level at-sensor radiance corresponding to

TABLE II
THE COMPARISON OF DIFFERENT SIMULATION METHOD

Items	RSISM	SENSOR	TIRSS	PICASSO	TCRS-INSAT3D	ETESS	Moon-based simulation
Suitable wavelength (μm)	0.5-1.75	0.4-2.5	0.76-1000	0.45-0.8	0.55-12.5	0.44-2.2	0.75-1000
Visible distance (km)	23	15	23	23	23	23	23
Aerosol type	rural	rural	MTF constant value	rural	rural	rural	rural
Solar zenith angle (°)	64.8	30		0	0~60	40	0-90
Simulation steps	1) Spectral simulation; 2) Atmospheric correction.	1) Determination of geometric relation; 2) Simulation of atmosphere effect and the at-sensor radiances; 3) Description of sensor hardware	1) Land surface scene simulation; 2) Atmospheric effect scene simulation; 3) Sensor imaging scene simulation	1) Convert input scene to reflectance; 2) Convert to TOA radiance; 3) Setup GENSAT viewing geometry; 4) Apply GENSAT STF; 5) Resample to GENSAT GSD; 6) Convert to photoelectrons; 7) Add noise; 8) Convert to voltage; 9) Analog-to-digital conversion.	1) Simulation of atmospheric contribution; 2) Calculation of satellite measurements	1) Sensor simulation; 2) The inversion process (reflectance retrieval).	1) Estimation of Moon-based imaging coverage; 2) Acquisition of radiation intensity at the entrance pupil; 3) Simulation of image output from Moon-based thermal infrared sensor.
Atmospheric radiative transfer	MTF/ MODTRAN	MODTRAN	LOWTRAN7 /MODTRAN/ MTF	MODTRAN	MODTRAN	MODTRAN	MODTRAN
Orbital height (km)	3	7.5	Space and Airborne	500	35700	705	380000

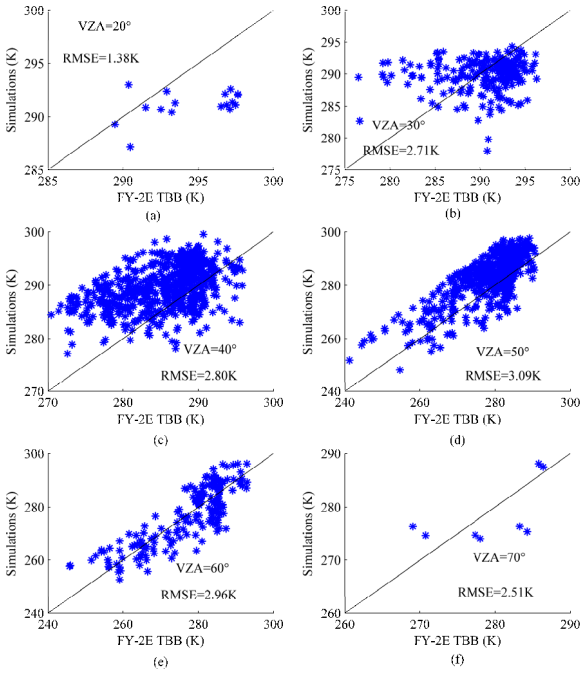

Fig. 10. Comparison of Moon-based thermal infrared simulations with FY-2E thermal infrared data. (a) The viewing zenith angles (VZA) is 20°; (b) VZA is 30°; (c) VZA is 40°; (d) VZA is 50°; (e) VZA is 60°; (f) VZA is 70°.

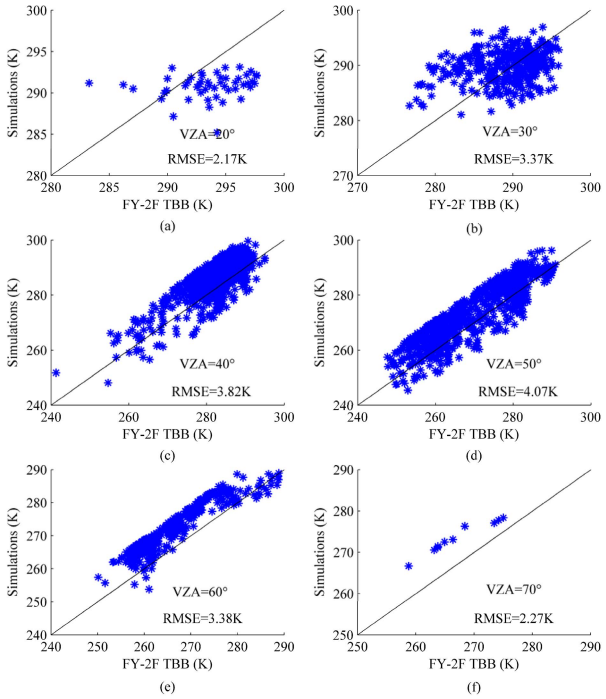

Fig. 11. Comparison of Moon-based thermal infrared simulations with FY-2F thermal infrared data. (a) The viewing zenith angles (VZA) is 20°; (b) VZA is 30°; (c) VZA is 40°; (d) VZA is 50°; (e) VZA is 60°; (f) VZA is 70°.

all four infrared channels of INSAT-3D Imager payload, and the INSAT-3D is geostationary satellite whose zenith angle is 0-60°. The Moon-based simulation has the largest range solar zenith angle with 0-90°. Every simulation method analyze the atmospheric effect and adopt the radiative transfer model MODTRAN, LOWTRAN, or Modulation transfer function (MTF). In theory, the zenith angle can affect the calculation of atmospheric radiative transfer, and the results of atmospheric parameters for Moon-based Earth observation change much in each image. The orbital height is 3, 7.5, space and airborne, 500, 35700, 705, and 380000 km, respectively. Overall, compared with the existing simulation method, the thermal infrared

imagery simulation from Moon-based Earth observation have large zenith angle and high orbital height, and analyzed the ionosphere effect based on the characteristics of Moon-based Earth observation platform.

VI. Conclusion

As a natural satellite of the Earth, the Moon has many superiorities compared with artificial satellites and can provide a new mean to monitor the LST due to the special orbital characteristics and orbit parameters of the Moon. However, Moon-based Earth observations are at the theoretical stage without actual Earth observations, and the observation performance needs to be explored by simulation. In this study, in view of the capability analysis of a Moon-based Earth observation platform in the thermal infrared band, a new method was developed to simulate thermal infrared images from Moon-based Earth observations. First, the viewing zenith angle and spatial coverage of Moon-based Earth observations were estimated using the JPL ephemeris data. Then, an atmospheric radiation transfer model MODTRAN was used to simulate the atmosphere influence on the Moon-based thermal infrared band and generate radiance images at the entrance pupil of the Moon-based Earth observation platform. Finally, thermal infrared images were obtained for the Moon-based Earth observation platform through the analysis of the thermal infrared optical sensor system and the grayscale quantization module of the Moon-based Earth observation platform.

Furthermore, the thermal infrared imaging results from the Moon-based observation platform were validated by the TBB data from the FY-2E and 2F satellites. The results show that the absolute error of Moon-based thermal infrared simulations is between 1.3-5.7 K, the RMSE is between 1.38 - 3.12 K, and the relative error is between 0.44% - 2.12%, indicating that the thermal infrared imaging model of the Moon-based Earth observation platform can realistically simulate the true conditions of the Earth surface and it is feasible for the Moon-based Earth observation platform to observe the Earth in the thermal infrared band. Moreover, this paper compared the thermal infrared imagery simulation from Moon-based Earth observation with six existing peer's simulation method for thermal infrared imagery, including RSISM, SENSOR approach, TIRSS, PICASSO, TCRS- INSAT3D, ETESS. In the future, research on the imaging parameter optimization of thermal infrared sensors in the Moon-based Earth observation platform will be carried out and provide support for the design and manufacture of thermal infrared sensors in the platform.

Acknowledgment

The authors are grateful to the National Aeronautics and Space Administration (NASA), National Oceanic and Atmospheric Administration (NOAA)–National Centers for Environmental Information and National Snow, and National Satellite Meteorological Center (NSMC) of the China Meteorological Administration (CMA) for providing MODIS, global land elevation data, and FY-2 VISSR data. They also grateful to teachers and students of their research group for providing writing assistance and support. They would also like to thank the anonymous reviewers for their voluntary work and the constructive comments which helped to improve the manuscript.

References

[1] E. Palle and P. R. Goode, "The lunar terrestrial observatory: Observing the Earth using photometers on the Moon's surface," *Adv. Space Res.*, vol. 43, no. 7, pp. 1083–1089, 2009.

[2] Y. X. Ding, H. D. Guo, and G. Liu, "Preliminary study on the performance of the moon-based ground observation synthetic aperture radar system," in *Proc. Abstr. 24th Nat. Space Explor. Academic Exchange Conf.*, 2011, pp. 1–8.

[3] D. W. Zhang, "Study on Moon-Earth observation methodology for global change," M.S. thesis, Dept. Geogr., East China Normal Univ., Shanghai, China, 2012.

[4] Y. X. Ding, H. D. Guo, and G. Liu, "Coverage performance analysis of Earth observation from lunar base for global change detection," *J. Hunan Univ. (Natural Sci.)*, vol. 41, no. 10, pp. 96–102, 2014.

[5] Y. X. Ding, H. D. Guo, and G. Liu, "Method to estimate the Doppler parameters of Moon-based SAR using JPL ephemeris," *J. Beijing Univ. Aeronaut. Astronaut.*, vol. 41, no. 01, pp. 71–76, 2015.

[6] H. Ye, H. Guo, G. Liu, Y. Ren, Y. Ding, and M. Lv, "Coverage analysis on global change sensitive regions from moon based observation," in *Proc. IEEE Int. Geosci. Remote Sens. Symp. (IGARSS)*, Jul. 2016, pp. 3734–3737.

[7] Y. Ren, H. Guo, G. Liu, and H. Ye, "Simulation study of geometric characteristics and coverage for Moon-based Earth observation in the electro-optical region," *IEEE J. Sel. Topics Appl. Earth Observ. Remote Sens.*, vol. 10, no. 6, pp. 2431–2440, Jun. 2017.

[8] H. Guo, H. Ye, G. Liu, C. Dong, and J. Huang, "Error analysis of exterior orientation elements on geolocation for a Moon-based Earth observation optical sensor," *Int. J. Digit. Earth*, vol. 13, no. 3, pp. 374–392, 2018.

[9] L. Yuan and J. Liao, "Exploring the influence of various factors on microwave radiation image simulation for moon-based Earth observation," *Frontiers Earth Sci.*, vol. 14, no. 2, pp. 430–445, Jun. 2020.

[10] T. Li, H. Guo, L. Zhang, C. Nie, J. Liao, and G. Liu, "Simulation of moon-based Earth observation optical image processing methods for global change study," *Frontiers Earth Sci.*, vol. 14, no. 1, pp. 236–250, Mar. 2020.

[11] L. Zhang, H. Guo, H. Jiao, G. Liu, G. Shen, and W. Wu, "A polar coordinate system based on a projection surface for moon-based Earth observation images," *Adv. Space Res.*, vol. 64, no. 11, pp. 2209–2220, Dec. 2019.

[12] K. Wu, C. Ji, L. Luo, and X. Wang, "Simulation study of moon-based InSAR observation for solid Earth tides," *Remote Sens.*, vol. 12, no. 1, p. 123, Jan. 2020.

[13] W. Duan, S. Huang, and C. Nie, "Entrance pupil irradiance estimating model for a moon-based Earth radiation observatory instrument," *Remote Sens.*, vol. 11, no. 5, p. 583, Mar. 2019.

[14] J. R. Schott, S. D. Brown, R. V. Raqueño, H. N. Gross, and G. Robinson, "An advanced synthetic image generation model and its application to multi/hyperspectral algorithm development," *Can. J. Remote Sens.*, vol. 25, no. 2, pp. 99–111, Jun. 1999.

[15] Z. T. Ye, X. F. Gu, X. L. Li, and Z. M. Wang, "Analysis of spectral characteristics among different sensors by use of simulated RS images," *Geo-Spatial Inf. Sci.*, vol. 24, no. 4, pp. 295–299, 2000.

[16] Z. T. Ye and X. F. Gu, "Simulation of remote sensing images based on MIVIS data," *Acta Geodaetica et Cartographic Sinica*, vol. 29, no. 3, pp. 235–239, 2000.

[17] A. Börner *et al.*, "SENSOR: A tool for the simulation of hyperspectral remote sensing systems," *ISPRS J. Photogramm. Remote Sens.*, vol. 55, nos. 5–6, pp. 299–312, Mar. 2001.

[18] G. J. Yang, Q. H. Liu, Q. Xiao, and W. J. Huang, "Mid-infrared atmosphere radiation transfer analytic model and remote sensing images simulation," *Spectrosc. Spectral Anal.*, vol. 29, no. 3, pp. 629–634, 2009.

[19] S. A. Cota, "PICASSO: An end-to-end image simulation tool for space and airborne imaging systems," *J. Appl. Remote Sens.*, vol. 4, no. 1, Jun. 2010, Art. no. 043535.

[20] A. C. Stephen *et al.*, "PICASSO: An end-to-end image simulation tool for space and airborne imaging systems II. Extension to the thermal infrared: Equations and methods," *Proc. SPIE*, vol. 4, no. 4, pp. 2840–2849, 2011.

[21] M. R. Pandya, D. B. Shah, H. J. Trivedi, and S. Panigrahy, "Simulation of at-sensor radiance over land for proposed thermal channels of imager payload onboard INSAT-3D satellite using MODTRAN model," *J. Earth Syst. Sci.*, vol. 120, no. 1, pp. 19–25, Feb. 2011.

[22] L. M. Zhao, "Thermal infrared radiance modeling of land surface background and imaging simulation," Ph.D. dissertation, Dept. Geogr. Inform. Sci., Nanjing Univ., Nanjing, China, 2011.
[23] K. Segl *et al.*, "End-to-end sensor simulation for spectral band selection and optimization with application to the Sentinel-2 mission," *Appl. Opt.*, vol. 51, no. 4, pp. 439–449, 2012.
[24] W. Verhoef and H. Bach, "Simulation of Sentinel-3 images by four-stream surface–atmosphere radiative transfer modeling in the optical and thermal domains," *Remote Sens. Environ.*, vol. 120, no. 10, pp. 197–207, 2012.
[25] J. Gastellu-Etchegorry, "Modeling radiative transfer in heterogeneous 3-D vegetation canopies," *Remote Sens. Environ.*, vol. 58, no. 2, pp. 131–156, Nov. 1996.
[26] J. P. Gastellu-Etchegorry *et al.*, "DART: 3-D model of optical satellite images and radiation budget," in *Proc. IEEE Int. Geosci. Remote Sens. Symp. (IGARSS)*, vol. 5, Jul. 2003, pp. 3242–3244.
[27] J. P. Gastellu-Etchegorry, E. Grau, and N. Lauret, "DART: A 3D model for remote sensing images and radiative budget of Earth surfaces," presented at the Arch. Ouverte HAL-IRD, Modeling Simulation Eng., C. Alexandru, Ed. London, U.K.: IntechOpen, Mar. 2012. [Online]. Available: https://www.intechopen.com/books/modeling-and-simulation-in-engineering/dart-model-remote-sensing-images-radiative-budget-and-energy-budget-of-earth-surfaces, doi: 10.5772/31315.
[28] W. Cui, W. Yi, Y. Qiao, L. Du, and X. Liu, "Thermal infrared imaging simulation for complex terrain," *Infr. Laser Eng.*, vol. 43, no. 10, pp. 3205–3210, 2014.
[29] H. Brooke, R. B. Megan, N. M. Jessica, L. M. Stephen, L. M. Michael, "Multimode imaging in the thermal infrared for chemical contrast enhancement. Part 2: Simulation driven design," *Anal. Chem.*, vol. 82, no. 20, pp. 8421–8426, 2010.
[30] H. Zhang, "Infrared thermal imaging detection and numerical simulation of the HuaShan rock painting stalactite diseases," in *Proc. Chin. Conf. Image Graph. Technol.*, 2013, pp. 232–242.
[31] S. Shi *et al.*, "Design of a novel substrate-free double-layer-cantilever FPA applied for uncooled optical-readable infrared imaging system," *IEEE Sensors J.*, vol. 7, no. 12, pp. 1703–1710, Dec. 2007.
[32] S.-L. Han, P. Zhang, and W.-L. Hu, "Infrared simulation of 4-bar target for the static performance evaluation of thermal imaging system," *Proc. SPIE*, vol. 8912, Aug. 2013, Art. no. 891204.
[33] C. Hausler, G. Milde, H. Balke, H.-A. Bahr, and G. Gerlach, "3-D modeling of pyroelectric sensor arrays part I: Multiphysics finite-element simulation," *IEEE Sensors J.*, vol. 8, no. 12, pp. 2080–2087, Dec. 2008.
[34] G. Milde, C. Hausler, G. Gerlach, H.-A. Bahr, and H. Balke, "3-D modeling of pyroelectric sensor arrays part II: Modulation transfer function," *IEEE Sensors J.*, vol. 8, no. 12, pp. 2088–2094, Dec. 2008.
[35] C. Nie, J. Liao, G. Shen, and W. Duan, "Simulation of the land surface temperature from moon-based Earth observations," *Adv. Space Res.*, vol. 63, no. 2, pp. 826–839, Jan. 2019.
[36] P. Coppo, L. Chiarantini, and L. Alparone, "Validation and simulation examples of an end-to-end simulator for optical imaging systems," *Proc. SPIE*, vol. 8889, no. 5, pp. 868–870, 2013.
[37] L. Guanter, K. Segl, and H. Kaufmann, "Simulation of optical remote-sensing scenes with application to the EnMAP hyperspectral mission," *IEEE Trans. Geosci. Remote Sens.*, vol. 47, no. 7, pp. 2340–2351, Jul. 2009.
[38] X. He and X. Xu, "Physically based model for multispectral image simulation of Earth observation sensors," *IEEE J. Sel. Topics Appl. Earth Observ. Remote Sens.*, vol. 10, no. 5, pp. 1897–1908, May 2017.
[39] C. Schueler and L. Woody, "Digital electro-optical imaging sensors," *Int. J. Imag. Syst. Technol.*, vol. 4, no. 3, pp. 170–200, 2010.
[40] Y. L. Gu, Y. L. Qiao, and W. N. Yi, "Application of satellite image in the scene simulation of thermal infrared," *Infr. Laser Eng.*, vol. 37, no. 2, pp. 248–250, 2008.
[41] E. P. Shettle and R. W. Fenn, "Models for the aerosols of the lower atmosphere and the effects of humidity variations on their optical properties," *Lancet*, vol. 48, no. 4068, p. 504, 1987.
[42] K. Bouchouicha and N. I. Bachari, "Simulation of a clear sky satellite image in water vapor and infrared satellite MSG channel's," *Revue des Energies Renouvelables*, vol. 15, no. 4, pp. 671–679, 2012.
[43] K. Segl *et al.*, "EeteS—The EnMAP end-to-end simulation tool," *IEEE J. Sel. Topics Appl. Earth Observ. Remote Sens.*, vol. 5, no. 2, pp. 522–530, Apr. 2012.
[44] K. Segl, L. Guanter, F. Gascon, T. Kuester, C. Rogass, and C. Mielke, "S2eteS: An end-to-end modeling tool for the simulation of Sentinel-2 image products," *IEEE Trans. Geosci. Remote Sens.*, vol. 53, no. 10, pp. 5560–5571, Oct. 2015.
[45] J. Gastellu-Etchegorry, E. Martin, and F. Gascon, "Dart: A 3-D model for simulating Satellite images and surface radiation budget," *Int. J. Remote Sens.*, vol. 25, no. 1, pp. 75–96, 2004.
[46] J. P. Gastellu-Etchegorry, "3D modeling of satellite spectral images, radiation budget and energy budget of urban landscapes," *Meteorol. Atmos. Phys.*, vol. 102, nos. 3–4, pp. 187–207, Dec. 2008.
[47] T. Yin, N. Lauret, and J.-P. Gastellu-Etchegorry, "Simulating images of passive sensors with finite field of view by coupling 3-D radiative transfer model and sensor perspective projection," *Remote Sens. Environ.*, vol. 162, pp. 169–185, Jun. 2015.
[48] L. F. Chen, J. L. Zhuang, and X. R. Xu, "The simulation of the thermal radiant directionality of continuous vegetation using Monte Carlo method," *J. Remote Sens.*, vol. 4, pp. 261–265, 2000.
[49] G. J. Yang, "Research on spaceborne high-resolution thermal infrared remote sensing imaging simulation," Ph.D. dissertation, Inst. Remote Sens. Appl., Chin. Acad. Sci., Beijing, China, 2008.
[50] D. Bulatov, E. Burkard, R. Ilehag, B. Kottler, and P. Helmholz, "From multi-sensor aerial data to thermal and infrared simulation of semantic 3D models: Towards identification of urban heat islands," *Infr. Phys. Technol.*, vol. 105, Mar. 2020, Art. no. 103233.

Jingjuan Liao received the B.S. and M.S. degrees in geoscience from Nanjing University, China, in 1987 and 1990, respectively, and the Ph.D. degree in geophysics from the Institute of Geophysics, Chinese Academy of Sciences, Beijing, China, in 1993. Since 2007, she has been a Professor working on microwave remote-sensing application with the Center for Earth Observation and Digital Earth and the Institute of Remote Sensing and Digital Earth, Chinese Academy of Sciences. She currently works with the Key Laboratory of Digital Earth Science, Aerospace Information Research Institute, Chinese Academy of Sciences. She has completed several research projects, and published more than 90 articles in relevant journals. Her current research interests include microwave scattering model, data processing, and surface parameters estimation.

Linan Yuan received the degree in surveying and mapping engineering from the China University of Mining and Technology, Beijing, China, in 2016. She is currently pursuing the Ph.D. degree with the Department of Geographical Information System, Aerospace Information Research Institute, Chinese Academy of Sciences, Beijing, and the University of Chinese Academy of Sciences, Beijing. Her current research interests include Moon-based Earth observation and microwave remote sensing.

Chenwei Nie received the graduate degree from the North China Institute of Aerospace Engineering, Langfang, China, in 2011, the master's degree from the China Three Gorges University, Yichang, China, in 2014, and the Ph.D. degree from the Department of Geographical Information System, Aerospace Information Research Institute, Chinese Academy of Sciences, Beijing, China, and the University of Chinese Academy of Sciences, Beijing, in 2019.